

## Simulation of Doppler Lidar Measurement Range and Data Availability

MATTHIEU BOQUET, PHILIPPE ROYER, JEAN-PIERRE CARIOU, AND MEHDI MACHTA

*Leosphere, Paris, France*

MATTHIEU VALLA

*ONERA, Palaiseau, France*

(Manuscript received 19 March 2015, in final form 14 March 2016)

### ABSTRACT

The measurement range of a coherent wind Doppler lidar (CWDL) along a laser beam is the maximum distance from the lidar where wind speed data are accurately retrieved. It means that, at this distance, a sufficient number of emitted laser photons are backscattered and received by the lidar. Understanding of the propagation of the laser through the atmosphere, and particularly the backscattering and extinction processes from aerosols, is therefore important to estimate the metrological performances of a CWDL instrument. The range is directly related to specific instrument characteristics and atmospheric content, such as the aerosols type, size, and density distributions. Associated with the measurement range is the notion of data availability, which can be defined, at a given range and over a time period, as the percentage number of data retrieved correctly by the CWDL over the total number of measurement attempts.

This paper proposes a new approach to predict the CWDL data availability and range of measurement using both instrumental simulation and atmospheric observations of aerosol optical properties from weather stations and simulations. This method is applied in several CWDL measurement campaigns during which estimated data availabilities and ranges are compared with the observations. It is shown that it is fairly possible to anticipate the data availability and the range coverage of CWDL technology at any site of interest where atmospheric data are available. The method also offers an additional way to diagnose the operation of the instrument and will help in the design of future instruments.

### 1. Introduction

For over 15 years, fiber-based lasers have been offering an effective technology to the lidar community, allowing new instruments to be designed at a lower price using off-the-shelf electronic components. The use of the double-clad fiber and the advances in semiconductor pump diode sources have allowed rapid power scaling of both pulsed and continuous fiber sources. The unique capabilities of fiber sources and amplifiers, coupled with significant commercial and academic progress in implementation, have driven fiber technology to enter active remote sensing markets (Valla 2005; Koroshetz 2005). The coherent wind Doppler lidar (CWDL) uses heterodyne detection by mixing (i.e., interfering) the laser light scattered from a remote target with a reference

local coherent laser oscillator. This technique offers high sensitivity and provides detailed phase and frequency information. Heterodyne detection outputs an electrical radio frequency beat note, providing information on the complex amplitude of the signal field. The reflectivity is calculated from the signal strength, the range is estimated from the time of flight, and the speed is calculated from the frequency or phase shift.

As a result of these technological and industrialization advancements, coherent wind Doppler lidars are nowadays being used on a regular basis in several research domains and industrial markets. For example, CWDLs are widely used in the wind energy industry for assessing wind as a resource (Clifton et al. 2013) and for evaluating the performance of wind turbine generators (Wagner 2010; Fleming et al. 2014). The success of these applications is largely dependent upon the data quality and availability of the CWDL, as poor measurement accuracy and low data availability will bias the results because

---

*Corresponding author address:* Matthieu Boquet, Leosphere, 43 rue de Liège, 75008 Paris, France.  
E-mail: mboquet@leosphere.com

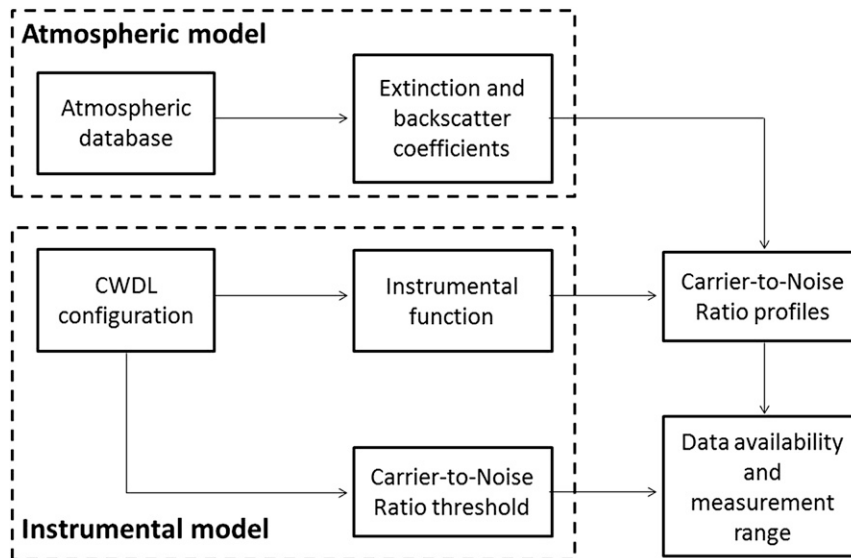


FIG. 1. Schematic diagram of the method used to simulate the data availability and measurement range of CWDL.

critical atmospheric features may be missed and thus not be taken into account in the performed analysis. CWDL data availability in the context of wind energy applications has already been presented by Aitken et al. (2012) and Davoust et al. (2014), in which the influence of atmospheric parameters like aerosols, temperature, and precipitation on the data availability has been studied. In aviation weather CWDLs are used to help aviation authorities in the design of optimal distance separation between two consecutive aircrafts at takeoff and landing as presented by Matayoshi and Yoshikawa (2015), for which the availability of measurements has a direct impact on the capacity of a CWDL to realize this functionality. In the context of operational meteorology, CWDLs are used to complement a network of instrumentation in which data are assimilated into weather forecast models (Illingworth et al. 2015). The variation of the instruments' data availability and the maximum range of measurement drive the quality of the forecast.

The data availability and the maximum measurement range of a CWDL are then crucial parameters to evaluate the lidar capacity to meet the main purposes of its application. Being able to predict CWDL data availability and the maximum range of measurement, according to instrumental parameters and local atmospheric conditions, will therefore allow for anticipating and understanding the applicability of a lidar at a given site. This paper describes a methodology to simulate and estimate the CWDL data availability and measurement range (section 2) and also provides validation results

against experimental field measurements and a detailed assessment of the method uncertainties, as well as examples of application (section 3).

## 2. Simulation of CWDL data availability and measurement range

### a. Description of the method

The schematic diagram describing the methodology developed for the simulation of CWDL data availability and measurement range is given in Fig. 1. The criteria used for the acceptance or rejection of CWDL measurements are based on the carrier-to-noise ratio (CNR) value (representing the signal-to-noise ratio for a modulated signal) and on the CNR threshold that is set to accept or reject the lidar measurement (CNR threshold calculation is described in section 2b). CNR is given at a distance  $r$  from the lidar using the following equation:

$$\text{CNR}(r) = F(r)\beta(r) \exp^{-2 \int_0^r \alpha(r') dr'}. \quad (1)$$

The instrumental function ( $F$ ) is determined using an instrumental model described in the next section. The instrumental function is assumed constant in time. The temporal fluctuations of the CNR values at each distance are due to variations of the aerosol extinction ( $\alpha$ ) and backscatter ( $\beta$ ) coefficients with time. The atmospheric model that provides the variations of  $\alpha$  and  $\beta$  in any part of the world is described in section 2c. Depending on the  $\alpha$  and  $\beta$  values at a given time and

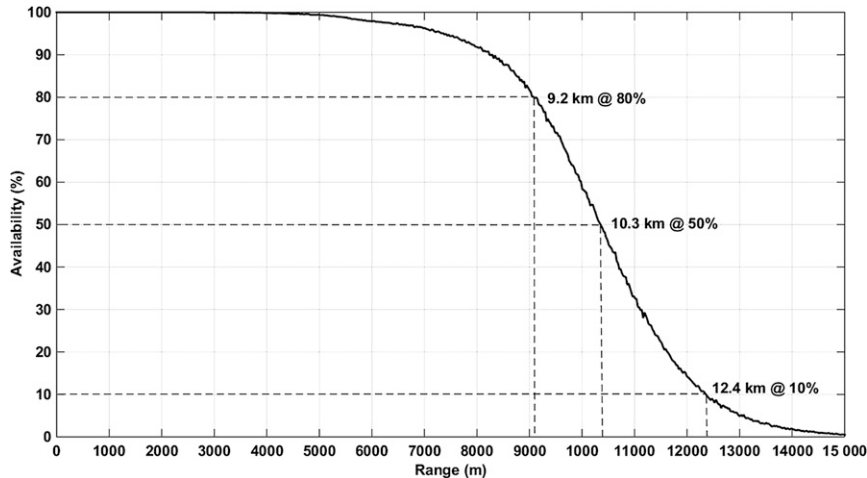


FIG. 2. Example of lidar data availability and measurement range for data availability of 80%, 50%, and 10% with a WINDCUBE 400S (100-m spatial resolution and 1-s accumulation time) at the Palaiseau site.

range, the CNR value may or may not exceed the CNR threshold.

Therefore, at each  $r$  the data availability over a given time period is defined as the percentage of instances when the CNR value exceeds the CNR threshold. The measurement range of the CWDL can be defined as the distance where the data availability falls below a certain percentage level. In this study we consider the measurement range for data availability levels of 80% (R80), 50% (R50), and 10% (R10). An example of lidar data availability for the Palaiseau, France, site with a WINDCUBE 400S commercialized by the company Leosphere is given in Fig. 2, where the corresponding measurement ranges were observed at 9.2, 10.3, and 12.4 km for data availability of 80%, 50%, and 10%, respectively.

### b. Instrumental model

The instrumental model is used to compute the instrumental function and to determine the CNR threshold of the CWDL.

The instrumental function ( $F$ ) of the CWDL is based on a propagation model of a Gaussian-focused beam (Targ et al. 1991):

$$F(r) = \frac{E\eta\lambda\pi\omega^2}{2h\text{BW}r^2} \left[ 1 + \left(1 - \frac{r}{F}\right)^2 \left(\frac{\pi\omega^2}{\lambda r}\right)^2 \right]^{-1}, \quad (2)$$

where  $h$  is Planck's constant ( $6.626 \times 10^{-34} \text{ J s}^{-1}$ ). In this equation the impact of the refractive index effect is neglected (this assumption is discussed in section 2d). The beam truncation can also be neglected because the dimensions of the receiving optics are much larger than the  $1/e^2$  intensity beam radius as explained in Targ et al. (1991).

The instrumental model allows for adapting the instrumental parameters to the CWDL configuration:

- Optical and detection parameters: optical/detection efficiency ( $\eta$ ), radius of curvature ( $F$ ), detection bandwidth (BW)
- Laser parameters: emitted wavelength ( $\lambda$ ),  $1/e^2$  intensity radius of the Gaussian beam ( $\omega$ ), laser-emitted energy ( $E$ )

The instrumental model is also used to determine the CNR threshold of the CWDL. This threshold depends on the lidar parameters [laser wavelength, number of fast Fourier transform (FFT) points, number of accumulated pulses, and sampling frequency] and the false alarm rate (FAR) associated with the measurement. The FAR is defined as the probability that a noise peak is detected as a valid Doppler peak in the spectra, and thus leads to report a false wind speed measurement as a valid measurement by the lidar. In this study, a 0.25% FAR was used. The theoretical CNR threshold is derived using lidar spectrum generated with the instrumental model. The spectrum simulation is based on the generation of a random covariance matrix as described in Odell and Feiveson (1966). Table 1 compares the measured and simulated CNR thresholds for different lidar configurations: a WINDCUBE 200S with a spatial resolution of 25, 50, and 100 m, and a WINDCUBE 400S with a spatial resolution of 100, 150, and 200 m (both instruments are based on the same architecture but have different pulse energy). Simulated and measured CNR thresholds are less than 1 dB apart. This result provides good confidence in the method of using simulated lidar spectra to determine the CNR threshold.

TABLE 1. Comparison of measured and simulated CNR thresholds for a 0.25% FAR.

CWDL system	Spatial resolution (m)	Measured CNR thresholds (dB)	Simulated CNR thresholds (dB)	Error measured – simulated CNR thresholds (dB)
WINDCUBE 200S	25	–25.9	–26.6	0.7
	50	–26.9	–27.5	0.6
	100	–28.6	–28.8	0.2
WINDCUBE 400S	100	–30.3	–30.4	0.1
	150	–28.4	–28.7	0.3
	200	–31.3	–31.1	–0.2

### c. Atmospheric model

For a given CWDL configuration, CNR values will vary with time and space as a function of atmospheric parameters  $\alpha$  and  $\beta$ . Neither parameter is routinely measured directly, but both can be indirectly estimated from either horizontal visibility  $V$  (expressed in meters) or aerosol optical depth (AOD) measurements.

Visibility measurements are widely used in meteorology and are, for instance, available in aviation routine weather reports (METARs; ICAO 2013). The model of Kim and McArthur (2001) can be used to convert  $V$  into ground-based  $\alpha$  for a given  $\lambda$ :

$$\alpha(z_0) = -\frac{\ln(0.02)}{V} \left( \frac{\lambda}{550 \text{ nm}} \right)^{-a}, \quad (3)$$

where  $a$  is the Ångström exponent (Ångström 1964) reflecting the wavelength dependency of the extinction coefficient and dependence on atmospheric scatterers:

$$a = -\frac{\log\left(\frac{\alpha_{\lambda 1}}{\alpha_{\lambda 2}}\right)}{\log\left(\frac{\lambda 1}{\lambda 2}\right)}. \quad (4)$$

Another way to derive the extinction coefficient at ground level is to use aerosol optical depth measurements. AOD values are extrapolated at  $\lambda$  with the Ångström exponent computed between two other wavelengths, and the extinction coefficient profile is finally derived assuming a linear decreasing distribution of the extinction coefficient through the planetary boundary layer height ( $z_{\text{PBL}}$ ). AOD measurements are available at several wavelengths from the Aerosol Robotic Network (AERONET; NASA GSFL 2006; Holben et al. 1998) sun photometers or from Monitoring Atmospheric Composition and Climate (MACC; ECMWF 2012) model outputs. AERONET is composed of  $\sim 400$  sun photometer stations distributed around the world. The MACC project

provides data records on atmospheric composition and especially aerosol distribution around the world with a spatial grid resolution of  $0.125^\circ$ . PBL heights are available in MACC outputs or can be derived from radiosounding profiles (e.g., Hennemuth and Lammert 2006). The conversion of AOD into ground-level aerosol extinction could be checked using visibility measurement, but it is not the purpose of this study. Nevertheless, the impact of this conversion on the estimation of the lidar data availability is discussed in section 3b.

The backscatter coefficient is directly linked to the extinction coefficient by the extinction-to-backscatter ratio or the so-called lidar ratio (LR). LR can be derived from the single-scattering albedo ( $w_0$ ) and the backscattering phase function ( $P_\pi$ ) provided by almucantar scans of AERONET sun photometers (Cattrall et al. 2005):

$$\beta = \frac{\alpha}{\text{LR}} \text{ with LR} = \frac{1}{4\pi} w_0 P_\pi. \quad (5)$$

These measurements are realized at 870 and 1020 nm, and then are extrapolated to  $\lambda$  using the same approach as for AOD measurements.

Examples of LR and extinction coefficient probability density functions (pdfs) derived from AERONET sun photometer measurements are given in Fig. 3 for Paris, France; Frankfurt, Germany; London, United Kingdom; Nice, France; Seoul, South Korea; and Beijing, China. The LR distributions are reasonably consistent between the different sites and are centered around 30 sr. The distribution for Nice shows LR values slightly lower compared to other sites due to the presence of marine aerosols. Extinction coefficient distributions are very similar for continental western European sites but higher values are observed for eastern Asian sites (Seoul and Beijing).

### d. Limitations of the method

The method developed to simulate the measurement range of CWDL has some limitations, which are discussed in this section for further improvement of the method.

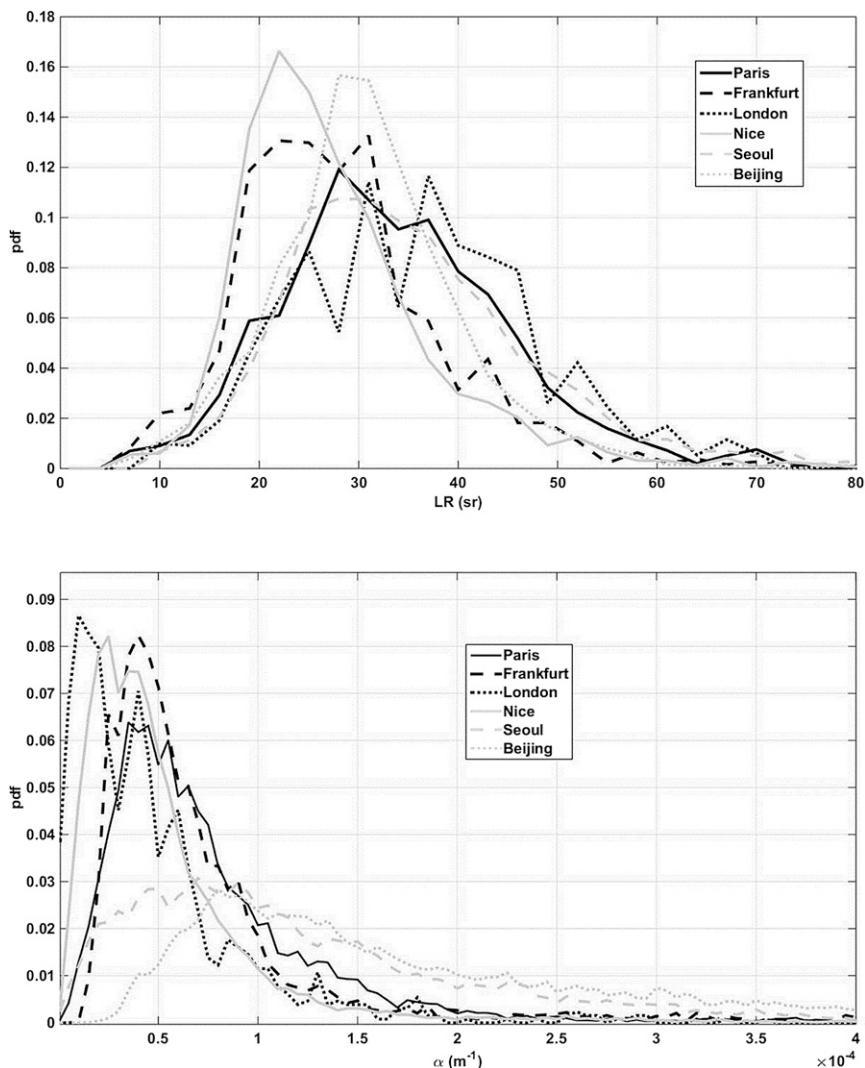


FIG. 3. Examples of (top) lidar ratio and (bottom) extinction coefficient pdfs derived from AERONET sun photometers at Paris, Frankfurt, London, Nice, Seoul, and Beijing.

The instrumental model used is valid only when the refractive index structure coefficient ( $C_n^2$ ) is low ( $<10^{-14} \text{ m}^{-2/3}$ ). This assumption is justified by the rapid decrease of  $C_n^2$  with height (Lawson and Carrano 2006). Nevertheless, the impact of the refractive index structure coefficient is taken into account in the uncertainty discussion when considering a variability of 10% in the output beam radius.

AOD, PBL, and LR data are given locally and are assumed to be representative of the surroundings where the lidar measurements are supposed to be made. Local effects or emissions affecting the lidar measurement range might not be captured in the MACC and AERONET data.

MACC simulations and AERONET measurements are not available in rainy or foggy conditions. These

atmospheric conditions are thus not taken into account in the measurement range simulation.

LR and AOD data provided by AERONET sun photometers are available only for daytime and clear-sky conditions. The MACC atmospheric database has the benefit of being available in both daytime and nighttime and in cloudy conditions.

### 3. Results

#### a. Uncertainty analysis

The main source of uncertainty for the simulation of the instrumental function is caused by the uncertainties in getting the correct value of some of the instrumental parameters. “Averaged,” “favorable,” and “unfavorable”

TABLE 2. Averaged, favorable, and unfavorable CWDL configurations used for the uncertainty analysis on instrumental parameters.

Instrumental parameters	Averaged configuration	Favorable configuration	Unfavorable configuration
Laser-emitted energy	Averaged value	Averaged value + 10%	Averaged value - 10%
Laser quality factor	Averaged value	Averaged value - 0.1	Averaged value + 0.1
$1/e^2$ intensity radius of the Gaussian beam	Averaged value	Averaged value + 10%	Averaged value - 10%
Instrumental defocus	Averaged value	Averaged value + 50 $\mu\text{m}$	Averaged value - 50 $\mu\text{m}$
Optical/detection efficiency	Averaged value	Averaged value + 10%	Averaged value - 10%

configurations of the lidar were simulated in which some of the hardware parameters were modified, such as the laser-emitted energy  $E$  ( $\pm 10\%$ ); the laser quality factor (ISO 2005), which is also known as the beam quality factor  $M^2$  ( $\pm 0.1$ );  $\omega$  ( $\pm 10\%$ ); the instrumental defocus ( $\pm 50 \mu\text{m}$ ); and optical/detection efficiency ( $\pm 10\%$ ). These different configurations are summarized in Table 2. The simulated

measurement range of data availability shows a variation of measurement range of less than 1 km between favorable and unfavorable configurations (see top panel of Fig. 4).

It should be noted that the LR and AOD values must be converted to the lidar wavelength. This conversion introduces a relative small uncertainty in LR and AOD values that is ignored in this analysis, as it is expected to

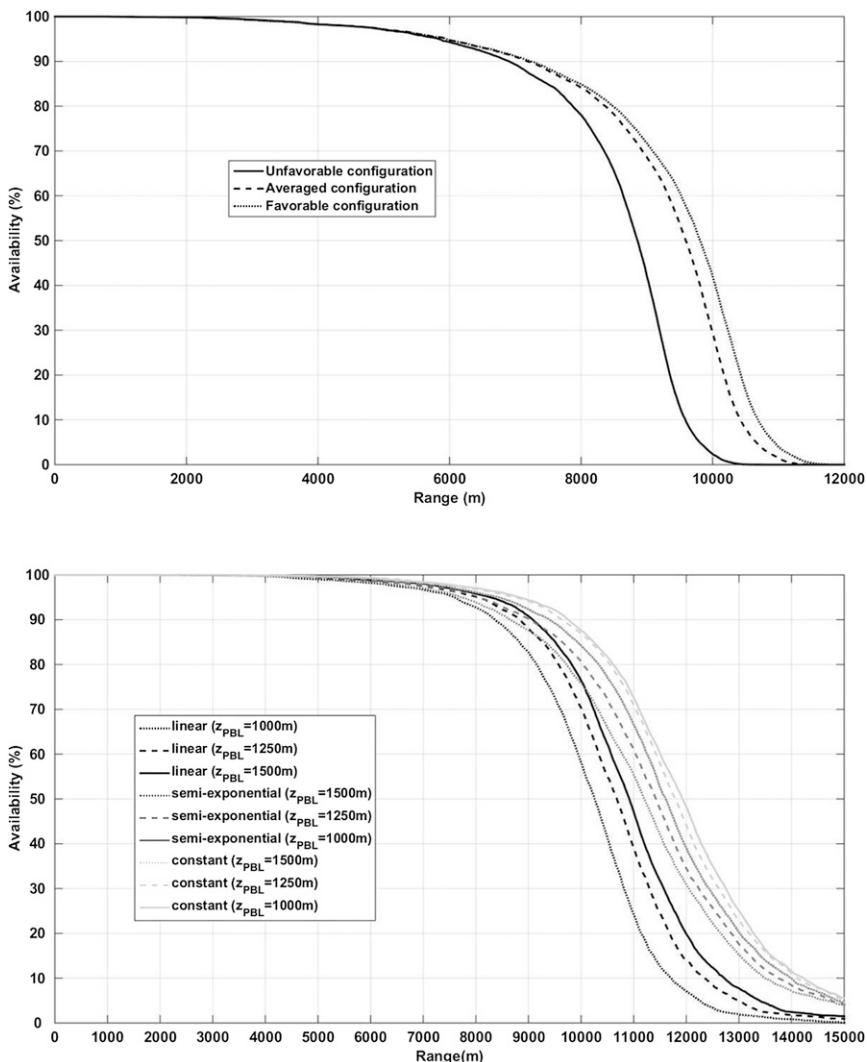


FIG. 4. Sensitivity of WINDCUBE 400S (200-m spatial resolution and 1-s accumulation time) data availability with (top) instrumental and (bottom) atmospheric parameters under Paris atmosphere.

TABLE 3. Mean extinction and backscatter coefficient values at ground level for different distribution models (linear, constant, semiexponential) and different PBL heights (1000, 1250, and 1500 m).

Distribution model	PBL height (m)	Mean extinction coefficient at ground level ( $\text{m}^{-1}$ )	Mean backscatter coefficient at ground level ( $\text{m}^{-1} \text{sr}^{-1}$ )
Linear	1000	$10.2 \times 10^{-5}$	$3.0 \times 10^{-6}$
	1250	$8.1 \times 10^{-5}$	$2.4 \times 10^{-6}$
	1500	$6.8 \times 10^{-5}$	$2.0 \times 10^{-6}$
Constant	1000	$5.0 \times 10^{-5}$	$1.5 \times 10^{-6}$
	1250	$4.0 \times 10^{-5}$	$1.2 \times 10^{-6}$
	1500	$3.3 \times 10^{-5}$	$1.0 \times 10^{-6}$
Semiexponential	1000	$3.3 \times 10^{-5}$	$1.0 \times 10^{-6}$
	1250	$2.8 \times 10^{-5}$	$0.8 \times 10^{-6}$
	1500	$2.5 \times 10^{-5}$	$0.7 \times 10^{-6}$

be small. The main source of uncertainty for the atmospheric model is due to the conversion of AOD values into extinction coefficient profiles. To evaluate the sensitivity to the atmospheric model, we simulated the data availability with different distribution models (linear, constant, and constant with an exponential decrease in the residual layer) and considered an uncertainty of 20% in PBL height. Ground-level extinction and backscatter coefficient values are summarized for the different atmospheric models in Table 3. Despite the high variation of extinction and backscatter coefficient (by a factor of 4 between the different models), the sensitivity to the atmospheric model and PBL height stays lower than 1.5 km for a data availability of 80% (bottom panel in Fig. 4).

#### b. Validation and extrapolation of the method

To validate the instrumental model, an experiment was conducted with a WINDCUBE 200S CWDL.

Horizontal scans (constant laser beam elevation) were performed in near-homogeneous atmospheric conditions. In such conditions the backscattering can be assumed constant, and the impact of the extinction can be neglected in the first kilometers of measurement [following Eq. (1), typical AOD values of 0.12 lead to a maximum CNR decrease of 1 dB up to a 4-km distance at 1543-nm laser wavelength]. The CNR-measured values can therefore be directly compared to the CNR modeled from the instrumental function in order to validate the model. Different focusing ranges are tested (400, 660, 1000, and 1400 m) and the results are compared with the simulated instrumental functions in Fig. 5. The instrumental function agrees well with the measurements, which proves that the instrumental model is able to reproduce the instrumental function in the different focus range settings.

Three validation sites were used to compare the measured and the data-simulated availability distributions

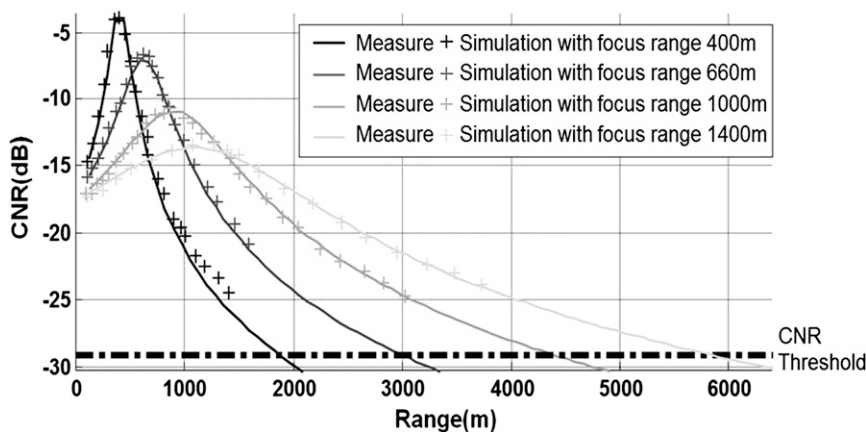


FIG. 5. Comparison of measured and simulated instrumental functions for a WINDCUBE 200S CWDL with a focusing range of 400, 660, 1000, and 1400 m.

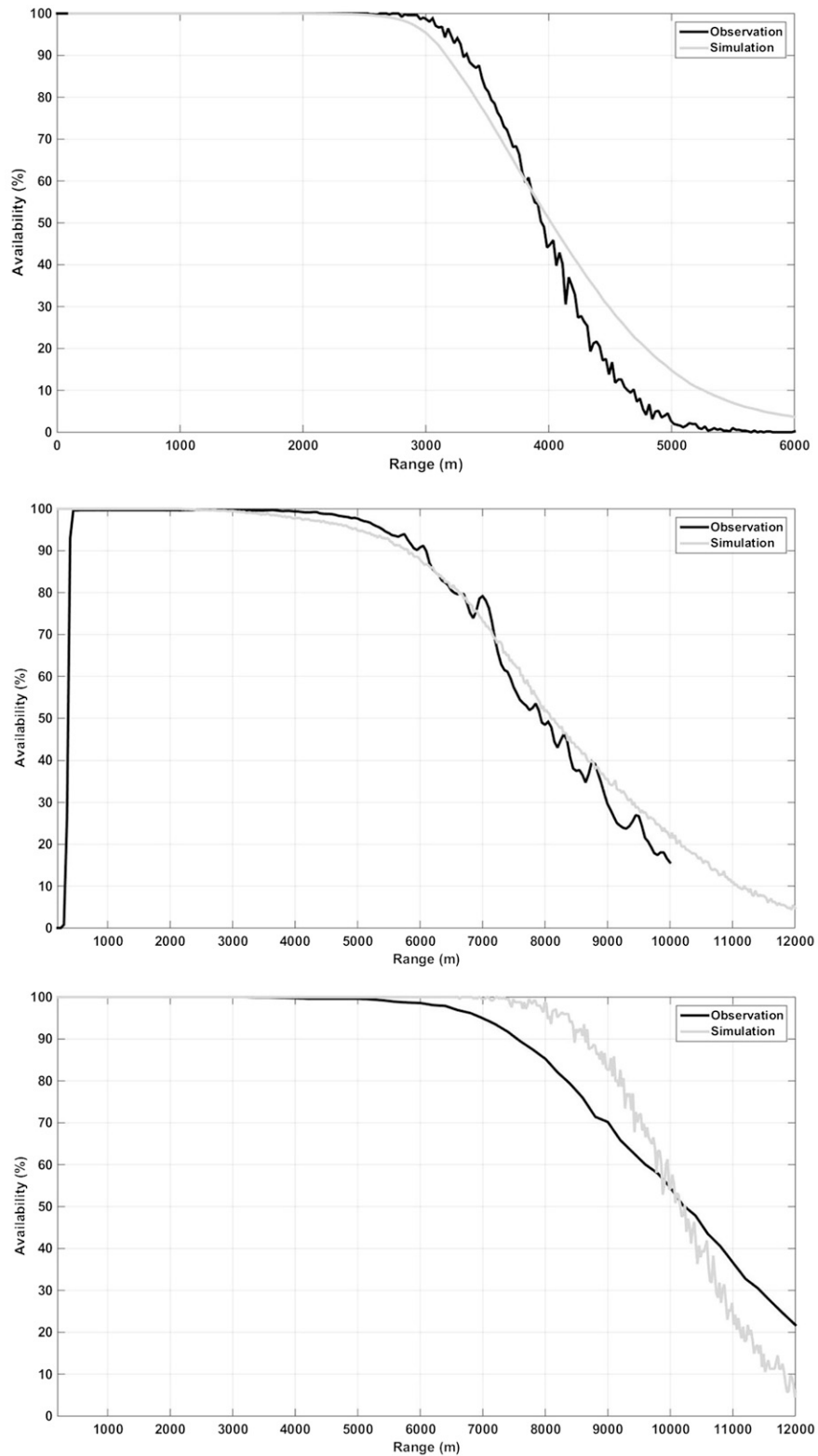


FIG. 6. Measured (black) and data-simulated (gray) availability distributions based on the available atmospheric data. (top to bottom) WINDCUBE 200S in Germany (1 month of data), WINDCUBE 400S in Southeast Asia (3 months of data), and WINDCUBE 400S in France (1 month of data).



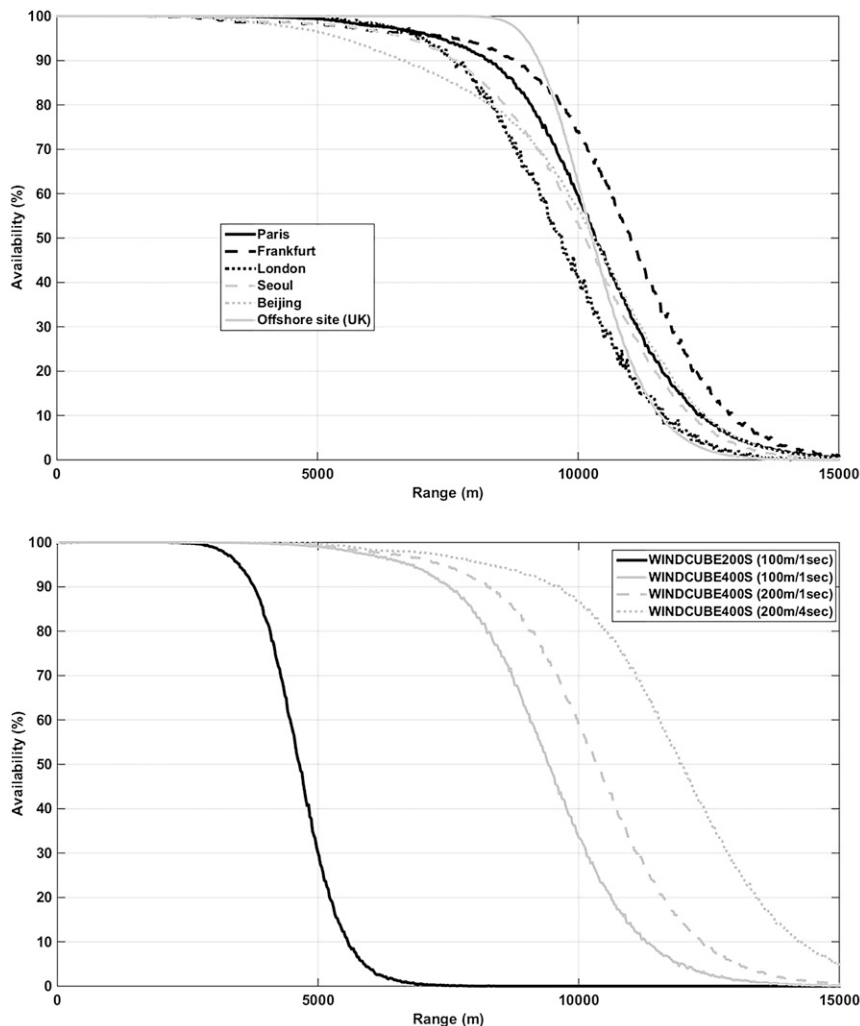


FIG. 7. Extrapolation of CWDL data availability (top) at different locations and (bottom) for various configurations.

(see Fig. 6). Atmospheric conditions were derived from AERONET measurement (for AOD and LR) and MACC outputs for the PBL height. A globally good agreement is observed with a maximum discrepancy of 1.5 km between the measurement and the simulation. A root-mean-square error of 230 m was observed for the WINDCUBE 200S in Germany, 250 m for the WINDCUBE 400S in Southeast Asia, and 675 m for the WINDCUBE 400S in France. The general slope of the data availability seems to be overestimated in the simulation. This may be due to an underestimation of the frequency of extreme atmospheric conditions from the simulation (very high and very low visibilities) that is probably due to local sources not captured by AERONET sun photometers. Nevertheless, the results are found to be consistent and within the uncertainty of the method discussed in the previous section.

The data availability has been extrapolated over 3 years (1 January 2010–1 January 2013) using the MACC dataset for different atmospheric conditions and lidar configurations (see Fig. 7). The MACC dataset has the advantage of being continuously available (in daytime and nighttime conditions) all over the globe. The measurement range—for example, for a data availability of 50% ( $R_{50}$ )—shows a variability of around 2 km among the different locations. The most favorable sites from those considered in this study are Frankfurt, the U.K. offshore site and Paris, whereas the lowest data availabilities are observed for London, Seoul, and Beijing. The data availability is also highly dependent upon the CWDL configuration (see bottom panel in Fig. 7). Under Paris atmospheric conditions, the  $R_{50}$  value is close to 5 km for a WINDCUBE 200S with a spatial resolution of 100 m

and a 1-s accumulation time, and close to 10.5 km for a WINDCUBE 400S with a spatial resolution of 200 m and a 1-s accumulation time.

#### 4. Conclusions

By modeling coherent wind Doppler lidar technology and simulating the laser beam propagation equation through the atmosphere, the estimation of the CWDL data availability and the measurement range can be derived. Despite the assumptions made on the aerosol data and the associated uncertainties, the estimated range compares well with the measured range on the test cases realized so far.

The methodology results in an estimation of the CWDL range distribution at a given site, averaged over several days or years. Shall one range result be given, it may be the distance reached at least a certain percentage of the time. For example, a 50% range (median range R50) means this distance is reached in average half of the time and not reached the other half. The 80% range (R80) is the distance where a wind speed value is correctly provided by the CWDL for 80% of the time, and we call it the maximum operational range. The 10% range (R10) would be considered the maximum measurement range obtainable.

Also, the availability of atmospheric data from weather stations (airports, AERONET, models, etc.) over a large part of the globe offers an interesting opportunity for developing the range estimation methodology further and allows for understanding and anticipating the CWDL range results prior and during the deployment of the instrument in the field.

*Acknowledgments.* This work was performed using results from MACC simulations (<http://www.gmes-atmosphere.eu>). MACC was funded by the European Commission under the EU Seventh Framework Programme, Contract 218793. We also thank AERONET (<http://aeronet.gsfc.nasa.gov/>) for collecting data around the world.

#### REFERENCES

- Aitken, L. M., M. E. Rhodes, and J. K. Lundquist, 2012: Performance of a wind-profiling lidar in the region of wind turbine rotor disks. *J. Atmos. Oceanic Technol.*, **29**, 347–355, doi:10.1175/JTECH-D-11-00033.1.
- Ångström, A., 1964: The parameters of atmospheric turbidity. *Tellus*, **16A**, 64–75, doi:10.1111/j.2153-3490.1964.tb00144.x.
- Cattrell, C., J. Reagan, K. Thome, and O. Dubovik, 2005: Variability of aerosol and spectral lidar and backscatter and extinction ratios of key aerosol types derived from selected Aerosol Robotic Network locations. *J. Geophys. Res.*, **110**, D10S11, doi:10.1029/2004JD005124.
- Clifton, A., D. Elliott, and M. Courtney, Eds., 2013: Ground-based vertically-profiling remote sensing for wind resource assessment. 1st ed. Expert Group Study on Recommended Practices, 15, International Energy Agency, 43 pp. [Available online at [https://www.ieawind.org/index\\_page\\_postings/RP%2015\\_RemoteSensing\\_1stEd\\_8March2013.pdf](https://www.ieawind.org/index_page_postings/RP%2015_RemoteSensing_1stEd_8March2013.pdf).]
- Davoust, S., A. K. Scholbrock, P. Fleming, A. Jéhu, M. Bardon, M. Bouillet, B. Vercherin, and A. Wright, 2014: Assessment and optimization of lidar measurement availability for wind turbine control. Preprints, *European Wind Energy Association 2014*, Barcelona, Spain, EWEA. [Available online at <http://www.nrel.gov/docs/fy14osti/61332.pdf>.]
- ECMWF, 2012: MACC-IFS NRT forecast of global total aerosol optical depth at multiple wavelengths, MACC-II products. [Available online at <http://apps.ecmwf.int/datasets/data/macc-nrealtime/levtype=sfc/>.]
- Fleming, P. A., A. K. Scholbrock, A. Jéhu, S. Davoust, E. Osler, A. D. Wright, and A. Clifton, 2014: Field-test results using a nacelle-mounted lidar for improving wind turbine power capture by reducing yaw misalignment. *J. Phys.: Conf. Ser.*, **524**, 012002, doi:10.1088/1742-6596/524/1/012002.
- Hennemuth, B., and A. Lammert, 2006: Determination of the atmospheric boundary layer height from radiosonde and lidar backscatter. *Bound.-Layer Meteor.*, **12**, 181–200, doi:10.1007/s10546-005-9035-3.
- Holben, B. N., and Coauthors, 1998: AERONET—A federated instrument network and data archive for aerosol characterization. *Remote Sens. Environ.*, **66**, 1–16, doi:10.1016/S0034-4257(98)00031-5.
- ICAO, 2013: *Meteorological Service for International Air Navigation*. 18th ed. Annex to the Convention on International Civil Aviation, 3, International Civil Aviation Organization, 208 pp.
- Illingworth, A. J., D. Cimini, C. Gaffard, M. Haefelin, V. Lehmann, U. Löhnert, E. J. O'Connor, and D. Ruffieux, 2015: Exploiting existing ground-based remote sensing networks to improve high-resolution weather forecasts. *Bull. Amer. Meteor. Soc.*, **96**, 2107–2125, doi:10.1175/BAMS-D-13-00283.1.
- ISO, 2005: Lasers and laser-related equipment—Test methods for laser beam widths, divergence angles and beam propagation ratios; Part 2: General astigmatic beams. Standard 11146-2:2005, International Organization for Standardization, 15 pp.
- Kim, I. I., and B. McArthur, 2001: Comparison of laser beam propagation at 785 nm and 1550 nm in fog and haze for optical wireless communications. *Optical Wireless Communications III*, E. J. Korevaar, Ed., International Society for Optical Engineering (SPIE Proceedings, Vol. 4214), doi:10.1117/12.417512.
- Koroshetz, J. E., 2005: Fiber lasers for lidar. *Proc. Optical Fiber Communication Conf. and Exposition and the National Fiber Optic Engineers Conf.*, Anaheim, CA, Optical Society of America, OFJ4. [Available online at <https://www.osapublishing.org/abstract.cfm?URI=OFC-2005-OFJ4>.]
- Lawson, J. K., and C. J. Carrano, 2006: Using historic models of Cn2 to predict r0 and regimes affected by atmospheric turbulence for horizontal, slant and topological paths. *Atmospheric Optical Modeling, Measurement, and Simulation II*, S. M. Hammel and A. Kohnle, Eds., International Society for Optical Engineering (SPIE Proceedings, Vol. 6303), 630304, doi:10.1117/12.679108.
- Matayoshi, A., and E. Yoshikawa, 2015: Dynamic wake vortex separation combining with AMAN/DMAN concept. *Proc. 15th*

- AIAA *Aviation Technology, Integration, and Operations Conf.*, Dallas, TX, AIAA, AIAA 2015-3397, doi:10.2514/6.2015-3397.
- NASA GSFL, 2006: Aeronet Robotic Network Data Download Tool, version 2. [Available online at <http://aeronet.gsfc.nasa.gov/>.]
- Odell, P. L., and A. H. Feiveson, 1966: A numerical procedure to generate a sample covariance matrix. *J. Amer. Stat. Assoc.*, **61**, 199–203, doi:10.1080/01621459.1966.10502018.
- Targ, R., M. J. Kavaya, R. M. Huffaker, and R. L. Bowles, 1991: Coherent lidar airborne windshear sensor: Performance evaluation. *Appl. Opt.*, **30**, 2013–2026, doi:10.1364/AO.30.002013.
- Valla, M., 2005: Study of a pulsed Doppler lidar based on an erbium fiber amplifier for wind field measurements in the boundary layer of the atmosphere (in French). Ph.D thesis, Ecole Nationale Supérieure des Télécommunications, 172 pp. [Available online at <http://www.theses.fr/2005ENST0030>.]
- Wagner, R., 2010: Accounting for the speed shear in wind turbine power performance measurement. Ph.D thesis, Risø National Laboratory for Sustainable Energy, 124 pp. [Available online at <http://orbit.dtu.dk/files/6433255/ris-phd-58.pdf>.]